Atomic Layer Deposition of Sodium Fluoride Thin Films

Running title: NaF ALD

Running Authors: Kuraitis et al.

Sara Kuraitis[1], Donghyeon Kang[2], Anil U. Mane[2], Hua Zhou[3], Jake Soares[1], Jeffrey W. Elam[2,a)] and Elton Graugnard[1,b)]

[1]Micron School of Materials Science & Engineering, Boise State University, 1910 University Dr., Boise, Idaho 83725

[2]Applied Materials Division, Argonne National Laboratory, 9700 S. Cass Ave, Argonne, Illinois 60439

[3]X-ray Science Division, Advanced Photon Source, Argonne National Laboratory, Lemont, IL 60439

[a)] Electronic mail: jelam@anl.gov,

[b)] Electronic mail: eltongraugnard@boisestate.edu

The need for advanced energy conversion and storage devices remains a critical challenge amid the growing worldwide demand for renewable energy. Metal fluoride thin films are of great interest for applications in lithium-ion and emerging rechargeable battery technologies, particularly for enhancing the stability of the electrode-electrolyte interface and thereby extending battery cyclability and lifetime. Reported within, sodium fluoride (NaF) thin films were synthesized via atomic layer deposition (ALD). NaF growth experiments were carried out at reactor temperatures between 175 and 250 °C using sodium *tert*-butoxide and HF-pyridine solution. The optimal deposition temperature range was 175–200 °C, and the resulting NaF films exhibited low roughness ($R_q \approx 1.6$ nm for films of ~8.5 nm), nearly stoichiometric composition (Na:F = 1:1.05), and a growth per cycle value of 0.85 Å/cycle on SiO_2 substrates. These results are encouraging for

future applications of NaF thin films in the development of improved energy capture and storage technologies.

I. INTRODUCTION

In the decades since their introduction and commercialization, lithium-ion batteries (LIBs) have dominated the rechargeable battery market. However, commercial LIBs suffer from high cost due to the limited availability of lithium resources across the world.[1] Sodium-ion batteries (SIBs) are among the emerging battery technologies viewed as promising alternatives to LIBs. Unlike lithium, sodium resources are widespread and include abundant supply in the world's oceans. SIBs are therefore expected to be relatively low cost and more environmentally friendly than current commercial LIBs.

SIBs operate on the same fundamental principles as LIBs, so they also experience many of the same problems, such as limited theoretical energy density, structural instability of anode/cathode materials, dendrite formation, and short cycle life. Significant progress has been made towards overcoming these challenges through concentrated research in LIBs, and similar approaches are being explored in the continued development of SIBs.[2-6] In particular, control over the electrolyte interfaces—both solid electrolyte interphase (SEI) layers at the anode and cathode-electrolyte interface (CEI)—is a key to improving battery performance and stability. In a common approach[7], ultra-thin layer coatings are introduced to form stable, ion-conductive interfaces between the electrolyte and the electrodes. Recently, atomic layer deposition (ALD) has been recognized as a promising method to deposit thin film electrode coatings, which must be pinhole-free in order to form stable interfaces.[6, 8-11] ALD is a

deposition technique that enables conformal coating of complex substrates with sub-nanometer thickness control.[12, 13] ALD utilizes cyclic self-limiting surface reactions of alternating doses of chemical precursor vapors that react with a substrate surface to form a thin film. Because ALD is self-limiting and conformal across complex substrate geometries, it is particularly well-suited for depositing artificial interface layers in emerging battery technologies, including three-dimensional nano-ribbon and carbon nanotube sponge electrodes.[6, 8-10]

Metal fluorides are one class of materials being explored for advanced battery applications, and have demonstrated promising results as both electrodes and solid electrolytes in LIBs.[14-17] Sodium fluoride (NaF) has shown utility in SIB applications as a cathode constituent material and as a solid-electrolyte interface layer on sodium metal anodes.[18, 19] NaF films have been deposited via CVD,[20-22] as well as sputtering and spin-coating for use in solar cells.[23-26] All of these deposition methods lack the conformality and sub-nanometer-level precision of ALD, and although ALD has been used in the synthesis of many metal fluorides, no such process has been reported for ALD of NaF.

In this work, we report the synthesis of NaF thin films via ALD using sodium *tert*-butoxide (NaO^{t}Bu) and HF-pyridine solution through the process illustrated in Figure 1. NaO^{t}Bu is an air-sensitive solid that has previously been used for ALD of sodium-oxide-containing materials,[27-30] and HF-pyridine solution has been used for ALD of many metal fluorides including lithium fluoride using lithium *tert*-butoxide.[16, 17] In situ process characterization with a quartz crystal microbalance (QCM) was utilized to establish process parameters for self-limiting surface chemistry. For ex situ film characterization, NaF films were deposited on Si(100) coupons terminated with a native oxide layer (~ 20

Å). Films were characterized using X-ray photoelectron spectroscopy (XPS), spectroscopic ellipsometry (SE), grazing incidence X-ray diffraction (GIXRD), atomic force microscopy (AFM), and scanning electron microscopy (SEM).

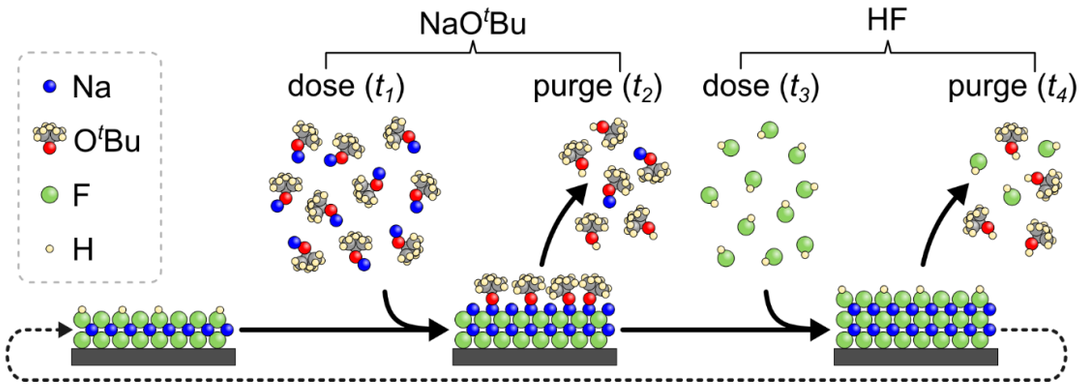

FIG. 1. Illustration of the ALD process for NaF using NaO^{t}Bu and HF-pyridine solution. Pyridine is not included in the schematic because it does not participate in the ALD surface reactions. The ALD cycle consists of four steps, each defined by a corresponding step time t_i: 1) NaO^{t}Bu dose, 2) purge, 3) HF-pyridine dose, 4) purge. Temporal separation of the precursor doses ensures that reactions occur only at the substrate surface (not in the vapor phase), and ultimate film thickness is therefore determined by the number of NaO^{t}Bu + HF-pyridine cycles completed.

II. EXPERIMENTAL

A. NaF Deposition

ALD was performed in a custom-built viscous flow reactor attached to an argon-filled glove box.[31] The argon-filled glove box was used to prevent the hygroscopic NaF from absorbing atmospheric H_2O vapor, which might change the properties of the films. The process was controlled and monitored using custom LabVIEW software. The reaction chamber—a 4.76 cm diameter stainless steel tube—was heated to 200 °C and

was maintained at ~1 Torr internal pressure with 270 sccm flow of ultra-high purity argon carrier gas (99.999% Ar). A subset of experiments was also performed at temperatures of 175 °C, 225 °C, and 250 °C to explore the temperature dependence of the ALD process. ALD experiments below a growth temperature of 175 °C were not attempted to avoid condensation of the NaO^{t}Bu compound. NaO^{t}Bu (97% purity, Sigma-Aldrich) is a white, crystalline powder with a melting point of 180 °C that adopts a hexamer structure and has a vapor pressure of 0.75 Torr at 140 °C.[30] The NaO^{t}Bu was contained in a custom-machined stainless-steel bubbler and heated to 130–140 °C bottom-of-pot temperature. NaO^{t}Bu was delivered to the reaction chamber by diverting 45 sccm Ar through the bubbler during each dose. HF-pyridine (~70% HF, ~30% pyridine, Sigma-Aldrich) was contained in an unheated stainless-steel cylinder (Swagelok). The NaF ALD cycle is defined by the NaO^{t}Bu dose time (t_1) and purge time (t_2), as well as the HF-pyridine dose time (t_3) and purge time (t_4), with the overall cycle timing denoted t_1–t_2–t_3–t_4. Although a range of dose and purge times were explored for both precursors, typical values were 3–20–2–15, where each time is measured in seconds.

B. Characterization

In situ quartz crystal microbalance (QCM) measurements were performed using a welded ALD sensor head (Inficon) with a 6 MHz RC-cut quartz crystal (Phillip Technologies). To minimize film deposition on the back side of the crystal, the sensor head was continually purged with Ar gas to bring the total chamber pressure up to ~1.1 Torr. The QCM was brought to thermal equilibrium in the reaction chamber over several hours, and the crystal was coated with ALD alumina (Al_2O_3) using alternating cycles of trimethylaluminum and H_2O prior to each NaF deposition to prepare a well-defined

starting surface for the NaF ALD. Frequency shifts due to film deposition were measured with an STM-2 Thin Film Rate/Thickness Monitor (Inficon). Mass changes per unit area (Δm) were calculated according to the Sauerbrey equation, as output by the STM-2 LabVIEW library supplied by Inficon.

For ex situ characterization, 100 ALD cycles of NaF were performed on Si(100) with ~ 20 Å native oxide (West Coast Silicon). To minimize air exposure prior to characterization, NaF-coated samples were stored under argon inside the reactor-attached glove box or in mylar bags heat-sealed inside of the glove box.

X-ray photoelectron spectrometry (XPS) measurements were performed on a Thermo Scientific K-Alpha XPS system operating in standard lens mode. The X-ray source was Al Kα with a spot size of 400 μm. Survey scans used a pass energy of 200.0 eV and step size of 1.000 eV, while high-resolution scans used a pass energy of 50.0 eV and step size of 0.100 eV. Five scans were averaged for each sample. The XPS data were analyzed using Thermo Scientific Avantage software, and all spectra were referenced to the adventitious C 1s peak (284.8 eV). Additional details on XPS analysis are provided in Supplemental Information S2.

Spectroscopic ellipsometry (SE) was used to determine film thickness. For NaF deposition on Si, measurements were performed on a J.A. Woollam alpha-SE ellipsometer, and data were collected in standard acquisition mode with a single scan at an incidence angle of 70.094° at 188 wavelength increments from 380 – 900 nm. For NaF deposition on Al_2O_3 coated Si, measurements were performed on a J.A. Woollam M-2000 ellipsometer, and data were collected at multiple angles with 328 wavelength steps from 380 – 900 nm. Analysis was performed using CompleteEASE 5.1 software. The

thicknesses of the native oxide layer (20.06 Å) and alumina layer (542 Å) were measured prior to NaF deposition, and the thickness of the deposited NaF layer was fit with a NaF Sellmeier model for bulk NaF provided in the material library of the CompleteEASE software.

Grazing incidence X-ray diffraction (GIXRD) experiments were performed at an undulator beamline 33-ID-D at the Advanced Photon Source (APS), Argonne National Laboratory on a six-circle *Kappa* goniometer with an X-ray energy of 10.5 keV using a pixel array area detector (Dectris Pilatus 100K). The incoming X-ray beam had a flux of 10^{12} photons per second. To optimize the thin film diffraction signal, a small angle of incidence near the substrate total reflection critical angle (e.g., 0.2-0.3º) was adopted for the GIXRD scans. NaF thin film samples were placed in a He flow cell during ex situ synchrotron GIXRD measurements to minimize air exposure.

Atomic force microscopy (AFM) images of NaF surfaces were obtained on Bruker Dimension FastScan AFMs equipped with Nanoscope V Controllers operating in peak-force tapping mode using ScanAsyst-Air-HR probes. As-deposited samples were stored in Ar and transferred in an Ar-filled vessel to an AFM housed in an Ar-filled MBraun3-glove glovebox. Additional air-exposed samples were removed from the Ar storage environment and imaged in ambient conditions after ~30 min of air exposure. AFM images were processed with Gwyddion 2.56.[32] Prior to root mean square roughness calculations, AFM images were leveled with a mean plane subtraction and row alignment (median subtraction) to remove scan line artifacts.

Scanning electron microscopy (SEM) was performed on an FEI Teneo FESEM using an in-column secondary electron detector (accelerating voltage = 1.00 kV, aperture

= 32 μm, working distance = 2.0 mm). Samples were stored in Ar and transported in an Ar-filled vessel before undergoing brief air exposure while being transferred into the SEM chamber.

III. RESULTS AND DISCUSSION

In situ QCM was used to establish precursor dose and purge times, and to examine steady-state growth behavior of the NaO^{t}Bu + HF-pyridine ALD chemistry. Steady-state growth for typical cycle timing of 3–20–2–15 at 200 °C is shown in Figure 2a, with two cycles shown in detail in Figure 2b.

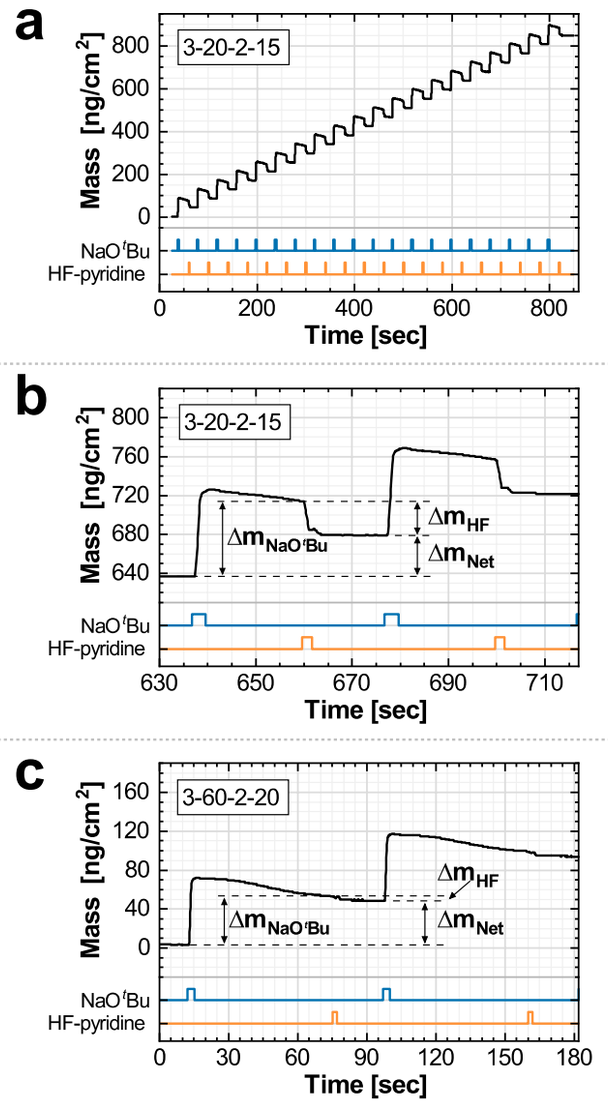

FIG. 2. QCM data for (a) steady-state NaF growth with 3–20–2–15 cycle timing, (b) detailed view of two cycles with 3–20–2–15 cycle timing, and (c) detailed view of two cycles with 3–60–2–20 cycle timing. The x- and y-scale values have been shifted so that both start at zero for the graphed data, though additional NaF cycles were completed prior those shown (in the case of Fig. 2a, 39 cycles were completed prior to the steady-state cycles shown). All QCM measurements were performed at 200 °C and normalized to QCM of alumina (trimethylaluminum + water) to correct for any back-side deposition on the QCM crystal.

For the last 15 ALD cycles shown in Fig. 2a (3–20–2–15 cycle timing), the NaO^{t}Bu half-cycle yielded an average mass change per unit area of Δm_{NaO^tBu} = 78 ng/cm^2 (std. dev. = 0.2 ng/cm^2), while the HF-pyridine half-cycle yielded a mass change of Δm_{HF} = −35 ng/cm^2 (std. dev. = 0.1 ng/cm^2). The average mass change for a complete ALD cycle was Δm_{Net} = 42 ng/cm^2 (std. dev. = 0.02 ng/cm^2). Assuming an upper bound film density of ρ_{film} = 2.56 g/cm^3 for bulk crystalline NaF, the expected thickness change can be calculated using $\rho_{film} = \Delta m_{cycle} / \Delta t_{cycle}$, to be $\Delta t_{cycle} \geq 1.7$ Å/cycle. Two cycles of 3–60–2–20 are shown in Figure 2c, illustrating markedly different mass change trends compared to Figures 2a,b. The initial mass gain from the NaO^{t}Bu dose was smaller and some mass was subsequently lost during the prolonged purge ($\Delta m_{NaO^tBu} \approx 50$ ng/cm^2), and the HF-pyridine dose yielded relatively little mass change ($\Delta m_{HF} \approx -5$ ng/cm^2). Interestingly, the net mass change for a complete ALD cycle remained similar ($\Delta m_{Net} \approx$ 45 ng/cm^2) despite the large change in the behavior of each half-cycle. As a variety of dose and purge times were explored, increased purge times following NaO^{t}Bu doses were observed to cause a distinct change in process behavior. QCM data for additional cycle timing variations is provided in Supplemental Information Fig. S1. As shown in Fig. S3, micro-dosing experiments revealed that NaO^{t}Bu doses were not self-limiting for pulse–purge times of 3–60. This phenomenon associated with prolonged NaO^{t}Bu purge time was further investigated by depositing 100 ALD cycles of NaF on silicon substrates to determine whether the observed differences in mass change behavior would correlate with differences in film properties. Film thickness and composition were nearly identical for films deposited at 200 °C with a variety of cycle timing variations (see XPS composition results in Supplemental Information Figs. S5, S8–S9 and spectroscopic

ellipsometry thickness results in Figs. S12, S14). We postulate that the mass loss during prolonged purges following each NaO^{t}Bu dose was due to the relatively slow decomposition and loss of *tert*-butoxide ligands, leaving dangling bonds on the surface that were able to react with subsequent repeated NaO^{t}Bu doses. However, following up with an HF-pyridine dose after the prolonged purge re-saturated the surface and yielded nearly identical net mass change and film properties, so this instability of the *tert*-butoxide ligands may be inconsequential for binary ALD of NaF at 200 °C.

We propose the following half-reactions of NaF ALD, analogous to those previously proposed for similar LiF ALD chemistry: [17]

$$-(H)_x^* + NaO^tBu \rightarrow Na(O^tBu)_{1-x}^* + xHO^tBu \quad (1)$$

$$Na(O^tBu)_{1-x}^* + HF \rightarrow NaF-(H)_x^* + (1-x)HO^tBu \quad (2)$$

where asterisks denote surface species. Defining R as the ratio between Δm_{NaO^tBu} and Δm_{Net} for the 3–20–2–15 cycle timing:

$$R = \Delta m_{NaO^tBu}/\Delta m_{Net} = 1.8 \quad (3)$$

This ratio can also be expressed in terms of the atomic weights of the species in Eqs. 1-2:

$$R = [73(1-x) + 23 - x] / 42 \quad (4)$$

Solving for x from Eqs. 3–4 yields $x = 0.26$, indicating an average of 26% of the *tert*-butoxide ligands were removed as *tert*-butanol during the NaO^{t}Bu half-cycle, while 74% were removed during the HF-pyridine half-cycle using the 3–20–2–15 cycle timing. For the 3–60–2–20 cycle timing, 67% and 33% were removed in the NaO^{t}Bu and HF-pyridine half-cycles, respectively. We note that the polymeric nature of the NaO^{t}Bu compound[30] may lead to mass changes associated with the adsorption and desorption of intact NaO^{t}Bu molecules and clusters that do not contribute to the ALD chemistry in Eqs. 1–2 and complicate interpretation of the QCM data.

NaF films for ex situ characterization were deposited on Si(100) coupons via 100 ALD cycles of NaO^{t}Bu + HF-pyridine with 3–20–2–15 cycle timing. X-ray photoelectron spectroscopy (XPS) revealed these films to be nearly stoichiometric NaF. Films grown at 175 °C and 200 °C yielded Na:F = 1:1.05, while those grown at 225 °C and 250 °C yielded atomic ratios of 1:1.02 and 1:0.97, respectively. Figure 3 shows survey spectra and narrow scans of the Na 1s and F 1s regions for NaF deposited at 200 °C with 3–20–2–15 cycle timing. Additional XPS spectra for NaF films deposited at 175 °C, 225 °C, and 250 °C are provided in Supplemental Information S2. The survey spectra showed incidental contamination with Ti (all samples) and Cl (225 °C and 250 °C samples), which were attributed to precursor interactions with previously deposited Ti- and Cl-containing materials on the reactor walls. The Si 2s and Si 2p peaks in the survey scans indicated XPS signal from the substrate were included in the spectra; consequently, the carbon and oxygen peaks likely included signal from the native oxide and pre-existing adventitious carbon layers on the Si(100) substrates. The relative intensities of the Si peaks were markedly higher for films deposited at 250 °C (Fig. S7a, inset), which we attribute to film porosity (Figs. 6d, S16d, S17d). Although some of the C and O signal may have been the result of incomplete ALD surface reactions or decomposition of *tert*-butoxide ligands, precise chemical state identification was confounded by substrate effects. However, the combined C and O content including substrate signal was low (equivalent homogeneous composition of < 4 at.% C and < 2.5 at.% O for all samples), and total carbon and oxygen contamination within the deposited NaF films is expected to be minimal.

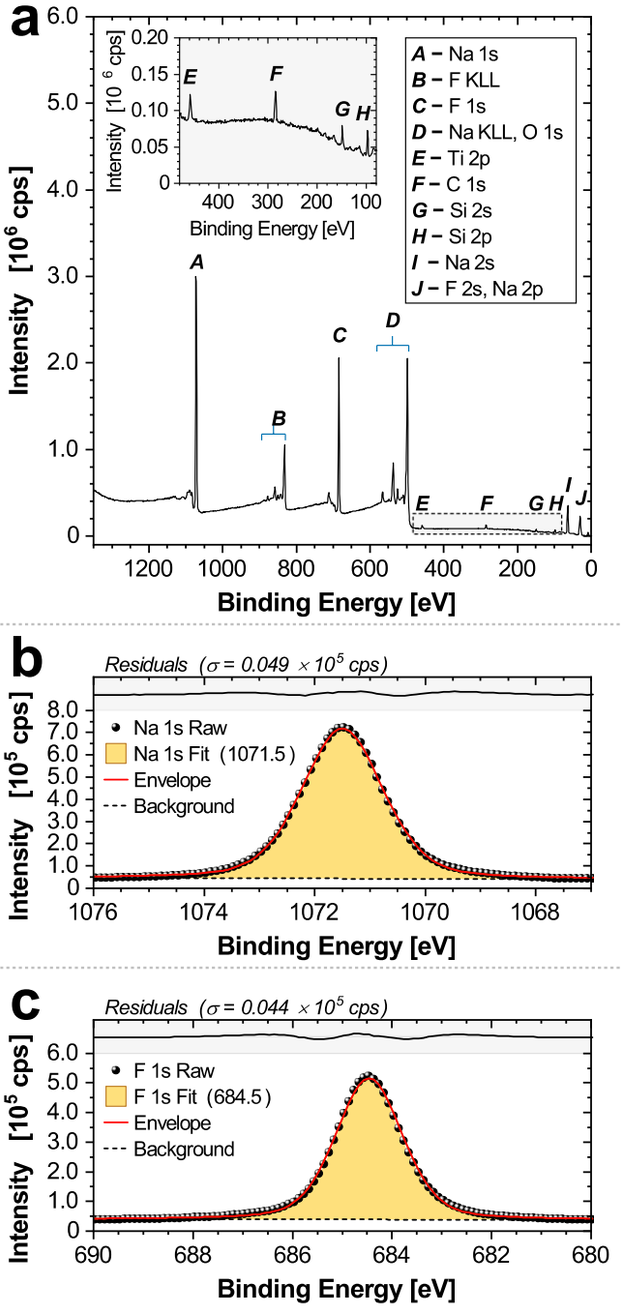

FIG. 3. XPS data and analysis results for NaF film on silicon substrates. Deposition was performed at 200 °C with 100 ALD cycles of NaO^tBu + HF-pyridine using 3–20–2–15 cycle timing. (a) Survey scan, (b) Sodium 1s region, (c) Fluorine 1s region.

NaF films for SE modelling were deposited on Si via 100 ALD cycles of NaO^{t}Bu + HF-pyridine with 3–20–2–15 cycle timing. Details on SE modelling and SE data for additional cycle timings are provided in the Supplemental Information S3. Total NaF film thickness for 100 ALD cycles of NaO^{t}Bu + HF-pyridine was ~85 Å at 175 °C and 200 °C and increased to ~90 Å and ~111 Å at 225 °C and 250 °C, respectively. Average NaF growth per cycle (GPC) for various growth temperatures is shown in Figure 4. Although all SE fits yielded mean squared error values less than 2, the NaF Sellmeier model deviated from measured Delta data at higher wavelengths for 250 °C samples (see Supplemental Information Fig. S13c–d). This discrepancy may be due to film non-uniformity (Fig. 6d, Supplemental Information Figs. S16d and S17d) and/or incidental chlorine contamination (Supplemental Information Fig. S7a) at higher growth temperatures. It should be noted that the GPC obtained from SE (~0.85 Å at 200 °C) is less than half of the minimum expected value based on QCM measurements (1.7 Å). This discrepancy might be attributed to differences in initial surface chemistry or crystallinity of the ALD NaF films, as the QCM crystal was coated with Al_2O_3 prior to each NaF deposition, while the silicon substrates with native oxide used for SE were directly coated with NaF. To explore this further, SE data were acquired for NaF deposited on Al_2O_3 coated Si at 200 ºC with 100 ALD cycles of NaO^{t}Bu + HF-pyridine with 3–20–2–15 cycle timing. The data, shown in Figure S15, confirm a higher GPC (~3.2 Å at 200 ºC) for growth on Al_2O_3, and additional work is needed to understand the differences in nucleation and growth between Al_2O_3 and SiO_2.

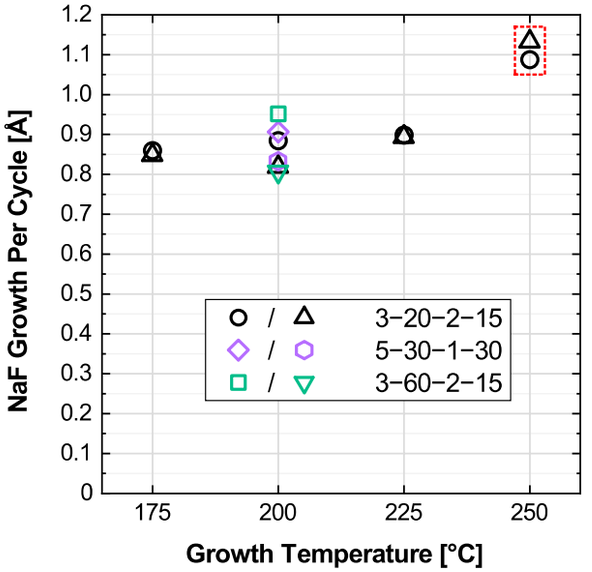

FIG. 4. Temperature dependence of NaF GPC, based on SE fitting results for 100 ALD cycles of NaO^{t}Bu + HF-pyridine on silicon substrates. Duplicate samples from different regions of the reactor chamber (separated by ~50 cm) are shown for each growth temperature. Calculated errors of the fitted thickness values are within the data markers. Films deposited at 250 °C (red) deviated slightly from the bulk NaF Sellmeier SE model, as shown in Supplemental Information Fig. S13c–d.

To characterize the structures of the deposited films, ex situ grazing incidence X-ray diffraction (GIXRD) measurements were performed for NaF films deposited on Si(100) coupons via 100 ALD cycles of NaO^{t}Bu + HF-pyridine with 3–20–2–15 cycle timing. The GIXRD data are shown in Figure 5 for samples grown at 175, 200, 225, and 250 ºC. Red ticks indicate the reflections for cubic NaF, which were computed using VESTA[33] using structure data for NaF (ICSD 53840).[34,35] For all deposition temperatures, the data indicate good agreement with the cubic NaF structure.

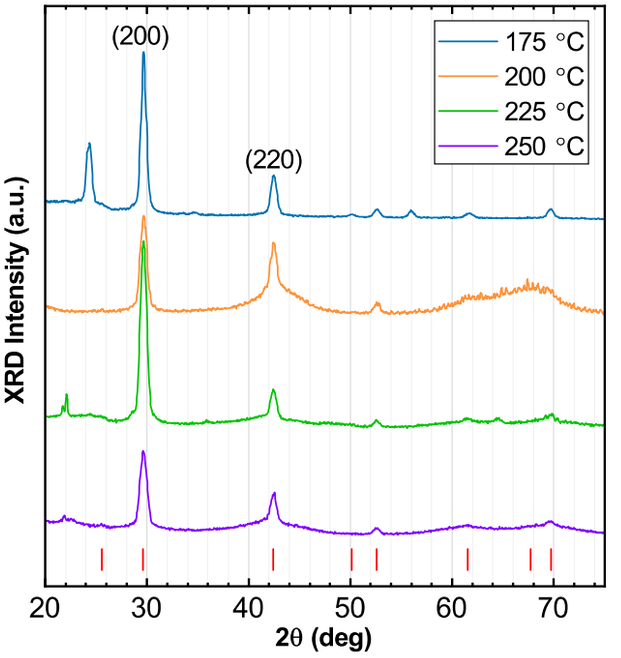

FIG. 5. Grazing incidence X-ray diffraction (GIXRD) data for NaF films deposited on silicon substrates with 100 ALD cycles of NaO^{t}Bu + HF-pyridine. Data are shown for films grown at 175, 200, 225, and 250 ºC, and red ticks indicate the predicted reflections for cubic NaF.

Finally, atomic force microscopy and scanning electron microscopy were used to characterize the film morphology. AFM images for as-deposited samples are shown in Figure 6 (see Supplemental Information S4 and S5 for AFM and SEM images of air-exposed samples). Root mean square roughness (R_q) values for the 175 °C and 200 °C as-deposited samples were both ~1.6 nm for films of roughly 8.5 nm as determined from SE of similar samples. Roughness values increased with temperature; the measured R_q values were ~2.2 nm at 225 °C for a film of ~9.0 nm thickness and ~5.8 nm at 250 °C for a film of 11.1 nm. We note that film thicknesses were measured in air using SE for samples equivalent to those measured via AFM, and that R_q values of several nm are

typical for polycrystalline ALD films in this thickness range, whereas amorphous ALD films in this thickness range exhibit R_q values well below 1 nm.[36] This finding is sensible given that NaF is an ionic solid and should readily crystallize even at low growth temperatures, as confirmed by GIXRD (Fig. 5). Air-exposed samples showed similar trends in roughness at elevated growth temperatures and had R_q values slightly higher than as-deposited samples (Fig. 6e). This increase in R_q for air-exposed films may be due to water adsorption. NaF is known to be hygroscopic and the adsorption of H_2O vapor from the ambient environment would cause volume expansion and an increase in surface roughness. Film morphology evolved with temperature, with small pores and cubic crystallite structures forming on the NaF surface at 250 °C, as shown in Fig. 6d (also Supplemental Information Figs. S16d, S17d). The pores may have resulted from de-wetting of the ALD NaF from the native silicon oxide surface at the higher growth temperatures.

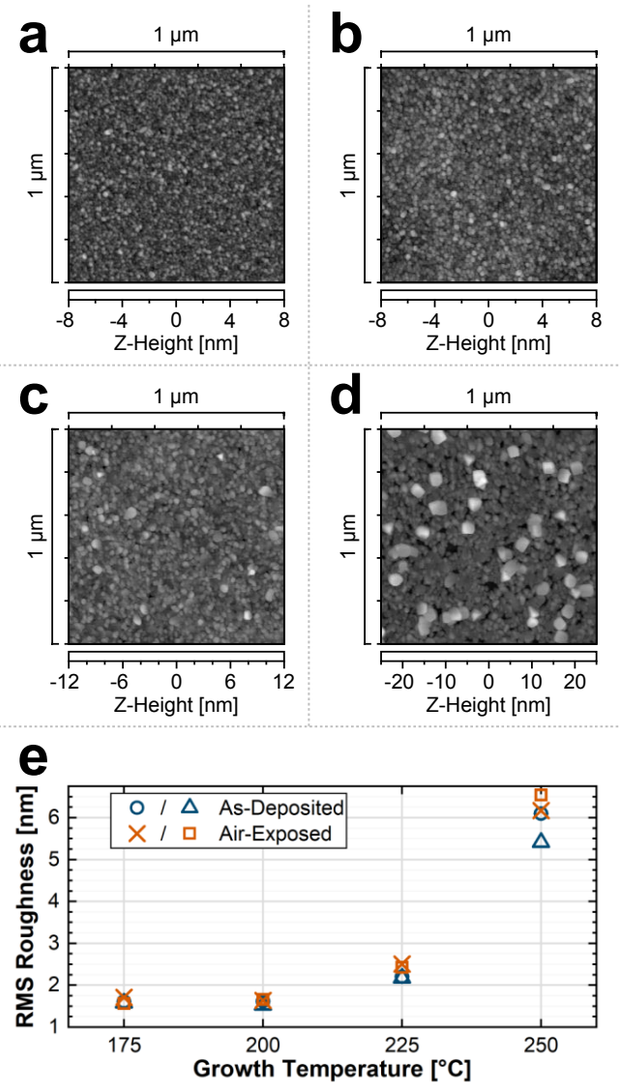

FIG. 6. Argon-filled glovebox AFM images of NaF surface morphology for as-deposited films on silicon substrates at growth temperatures of (a) 175 °C, (b) 200 °C, (c) 225 °C, and (d) 250 °C. (e) Surface roughness R_q values for various growth temperatures (blue = as-deposited, orange = air-exposed). See Supplemental Information S4 for AFM images of air-exposed samples.

IV. SUMMARY AND CONCLUSIONS

We reported a binary chemistry for ALD of NaF with an optimal growth temperature of 175–200 °C. Films deposited in this temperature range were polycrystalline with a cubic crystal structure, had an atomic ratio of Na:F = 1:1.05, and surface roughness of 1.6 nm for 8.5 nm thick films on Si. Optical properties were consistent with bulk values and growth per cycle was roughly 0.85 Å on Si and up to 3.2 Å on Al_2O_3. Films grown on Si at higher temperatures of 225–250 °C had increased surface roughness (2.2 and 5.8 nm, respectively), with pores and cubic surface crystallites forming at 250 °C. Standard timing for the NaO^{t}Bu + HF-pyridine ALD cycle was 3–20–2–15s. Increased purge time following the NaO^{t}Bu dose led to the decomposition and loss of O^{t}Bu ligands from the growth surface, but binary NaF ALD was largely unaffected by the instability of O^{t}Bu groups as subsequent HF-pyridine doses re-saturated the growth surface. These results may offer significant benefit for applications of NaF thin films in applications for both solar cells and advanced batteries.

ACKNOWLEDGMENTS

The work of A.M., D.K., and J.E. was supported as part of the Center for Electrochemical Energy Science, an Energy Frontier Research Center funded by the U.S. Department of Energy, Office of Science, Office of Basic Energy Sciences. The work of S.K., J.S., and E.G. at Boise State University was supported by Department of Energy Award no. DE-SC0019121. Atomic force microscope images were obtained in the Surface Science Laboratory at Boise State University (special thanks to Sophia Mitchell and Audrey

Parker for collecting glovebox AFM images). Scanning electron microscopy images were obtained by Dr. Nick Bulloss at the Boise State Center for Materials Characterization. This research used the beamline sector 33-ID-D of the Advanced Photon Source, a U.S. Department of Energy (DOE) Office of Science User Facility, operated for the DOE Office of Science by Argonne National Laboratory under Contract No. DE-AC02-06CH11357. Extraordinary facility operations were supported in part by the DOE Office of Science through the National Virtual Biotechnology Laboratory, a consortium of DOE national laboratories focused on the response to COVID-19, with funding provided by the Coronavirus CARES Act. S.K. and E.G. acknowledge Dr. Steven Hues and Dr. Kent Zhuang for valuable discussions of XPS.

DATA AVAILABILITY

The data that support the findings of this study are available within the article and its supplemental material. See supplementary material at [URL will be inserted by AIP Publishing] for additional QCM and XPS data, spectroscopic ellipsometry data, ambient AFM images, and SEM images.

[1]F. Wu, J. Maier and Y. Yu, Chemical Society Reviews **49** (5), 1569-1614 (2020).

[2]M. Walter, M. V. Kovalenko and K. V. Kravchyk, New Journal of Chemistry **44** (5), 1677-1683 (2020).

[3]W. Luo, F. Shen, C. Bommier, H. Zhu, X. Ji and L. Hu, Accounts of Chemical Research **49** (2), 231-240 (2016).

[4]X. Pu, H. Wang, D. Zhao, H. Yang, X. Ai, S. Cao, Z. Chen and Y. Cao, Small **15** (32), 1805427 (2019).

[5]J. Biemolt, P. Jungbacker, T. van Teijlingen, N. Yan and G. Rothenberg, Materials **13** (2) 425 (2020).

[6]F. Yu, L. Du, G. Zhang, F. Su, W. Wang and S. Sun, Advanced Functional Materials **30** (9), 1906890 (2020).

[7]D. Zuo, G. Tian, X. Li, D. Chen and K. Shu, Journal of Alloys and Compounds **706**, 24-40 (2017).

[8]B. Ahmed, C. Xia and H. N. Alshareef, Nano Today **11** (2), 250-271 (2016).

[9]Y. Zhao, K. Zheng and X. Sun, Joule **2** (12), 2583-2604 (2018).

[10]J. Liu, H. Zhu and M. H. A. Shiraz, Frontiers in Energy Research **6** (10) (2018).

[11]L. Ma, R. B. Nuwayhid, T. Wu, Y. Lei, K. Amine and J. Lu, Advanced Materials Interfaces **3** (21), 1600564 (2016).

[12]T. Kääriäinen, D. Cameron, M. L. Kääriäinen and A. Sherman, *Atomic Layer Deposition: Principles, Characteristics, and Nanotechnology Applications*, 2 ed. (Scrivener Publishing, Beverly, MA, 2013).

[13]S. M. George, Chemical Reviews **110** (1), 111-131 (2010).

[14]M. Mäntymäki, M. Ritala and M. Leskelä, Coatings **8** (8) 277 (2018).

[15]M. Feinauer, H. Euchner, M. Fichtner and M. A. Reddy, ACS Applied Energy Materials **2** (10), 7196-7203 (2019).

[16]Y. Lee, H. Sun, M. J. Young and S. M. George, Chemistry of Materials **28** (7), 2022-2032 (2016).

[17]L. Chen, K.-S. Chen, X. Chen, G. Ramirez, Z. Huang, N. R. Geise, H.-G. Steinrück, B. L. Fisher, R. Shahbazian-Yassar, M. F. Toney, M. C. Hersam and J. W. Elam, ACS Applied Materials & Interfaces **10** (32), 26972-26981 (2018).

[18]I. Hwang, S.-K. Jung, E.-S. Jeong, H. Kim, S.-P. Cho, K. Ku, H. Kim, W.-S. Yoon and K. Kang, Nano Research **10** (12), 4388-4397 (2017).

[19]Z. W. Seh, J. Sun, Y. Sun and Y. Cui, ACS Cent Sci **1** (8), 449-455 (2015).

[20]R. Binions, C. J. Carmalt and I. P. Parkin, Thin Solid Films **469-470**, 416-419 (2004).

[21]L. J. Lingg, A. D. Berry, A. P. Purdy and K. J. Ewing, Thin Solid Films **209** (1), 9-16 (1992).

[22]J. A. Samuels, W.-C. Chiang, C.-P. Yu, E. Apen, D. C. Smith, D. V. Baxter and K. G. Caulton, Chemistry of Materials **6** (10), 1684-1692 (1994).

[23]C. Andres, T. Schwarz, S. G. Haass, T. P. Weiss, R. Carron, R. Caballero, R. Figi, C. Schreiner, M. Bürki, A. N. Tiwari and Y. E. Romanyuk, Solar Energy **175**, 94-100 (2018).

[24]N. Li, S. Tao, Y. Chen, X. Niu, C. K. Onwudinanti, C. Hu, Z. Qiu, Z. Xu, G. Zheng, L. Wang, Y. Zhang, L. Li, H. Liu, Y. Lun, J. Hong, X. Wang, Y. Liu, H. Xie, Y. Gao, Y. Bai, S. Yang, G. Brocks, Q. Chen and H. Zhou, Nature Energy **4** (5), 408-415 (2019).

[25]G. Rajan, B. Belfore, S. Karki, D. Poudel, H. Kahoui, N. Lanham, E. Palmiotti, S. Soltanmohammad, A. Rockett and S. Marsillac, Thin Solid Films **690**, 137526 (2019).

[26]D. Ledinek, J. Keller, C. Hägglund, W.-C. Chen and M. Edoff, Thin Solid Films **683**, 156-164 (2019).

[27]H. H. Sønsteby, O. Nilsen and H. Fjellvåg, Journal of Vacuum Science & Technology A **34** (4), 041508 (2016).

[28]H. H. Sønsteby, O. Nilsen and H. Fjellvåg, Global Challenges **3** (10), 1800114 (2019).

[29]E. Østreng, H. H. Sønsteby, S. Øien, O. Nilsen and H. Fjellvåg, Dalton Transactions **43** (44), 16666-16672 (2014).

[30]H. H. Sønsteby, J. E. Bratvold, V. A. L. K. Killi, D. Choudhury, J. W. Elam, H. Fjellvåg and O. Nilsen, Journal of Vacuum Science & Technology A **38** (6), 060804 (2020).

[31]J. W. Elam, M. D. Groner and S. M. George, Review of Scientific Instruments **73** (8), 2981-2987 (2002).

[32]D. Nečas and P. Klapetek, Open Physics **10** (1), 181-188 (2012).

[33]K. Momma and F. Izumi, Journal of Applied Crystallography 44 (6), 1272-1276 (2011).

[34]G. Bergerhoff, I. Brown and F. Allen, International Union of Crystallography, Chester 360, 77-95 (1987).

[35]P. Debye and P. Scherrer, Physikalische Zeitschrift 19, 474-483 (1918).

[36]J. W. Elam, Z. A. Sechrist and S. M. George, Thin Solid Films **414** (1), 43-55 (2002).

List of Figure Captions:

FIG. 1. Illustration of the ALD process for NaF using NaO^{t}Bu and HF-pyridine solution. Pyridine is not included in the schematic because it does not participate in the ALD surface reactions. The ALD cycle consists of four steps, each defined by a corresponding step time t_i: 1) NaO^{t}Bu dose, 2) purge, 3) HF-pyridine dose, 4) purge. Temporal separation of the precursor doses ensures that reactions occur only at the substrate surface (not in the vapor phase), and ultimate film thickness is therefore determined by the number of NaO^{t}Bu + HF-pyridine cycles completed.

FIG. 2. QCM data for (a) steady-state NaF growth with 3–20–2–15 cycle timing, (b) detailed view of two cycles with 3–20–2–15 cycle timing, and (c) detailed view of two cycles with 3–60–2–20 cycle timing. The x- and y-scale values have been shifted so that both start at zero for the graphed data, though additional NaF cycles were completed prior those shown (in the case of Fig. 2a, 39 cycles were completed prior to the steady-state cycles shown). All QCM measurements were performed at 200 °C and normalized to QCM of alumina (trimethylaluminum + water) to correct for any back-side deposition on the QCM crystal.

FIG. 3. XPS data and analysis results for NaF film on silicon substrates. Deposition was performed at 200 °C with 100 ALD cycles of NaO^{t}Bu + HF-pyridine using 3–20–2–15 cycle timing. (a) Survey scan, (b) Sodium 1s region, (c) Fluorine 1s region.

FIG. 4. Temperature dependence of NaF GPC, based on SE fitting results for 100 ALD cycles of NaO^{t}Bu + HF-pyridine on silicon substrates. Duplicate samples from different regions of the reactor chamber (separated by ~50 cm) are shown for each growth temperature. Calculated errors of the fitted thickness values are within the data markers. Films deposited at 250 °C (red) deviated slightly from the bulk NaF Sellmeier SE model, as shown in Supplemental Information Fig. S13c–d.

FIG. 5. Grazing incidence X-ray diffraction (GIXRD) data for NaF films deposited on silicon substrates with 100 ALD cycles of NaO^{t}Bu + HF-pyridine. Data are shown for films grown at 175, 200, 225, and 250 ºC, and red ticks indicate the predicted reflections for cubic NaF.

FIG. 6. Argon-filled glovebox AFM images of NaF surface morphology for as-deposited films on silicon substrates at growth temperatures of (a) 175 °C, (b) 200 °C, (c) 225 °C, and (d) 250 °C. (e) Surface roughness R_q values for various growth temperatures (blue = as-deposited, orange = air-exposed). See Supplemental Information S4 for AFM images of air-exposed samples.

Journal of Vacuum Science Technology A

PLEASE CITE THIS ARTICLE AS DOI: 10.1116/6.0000847

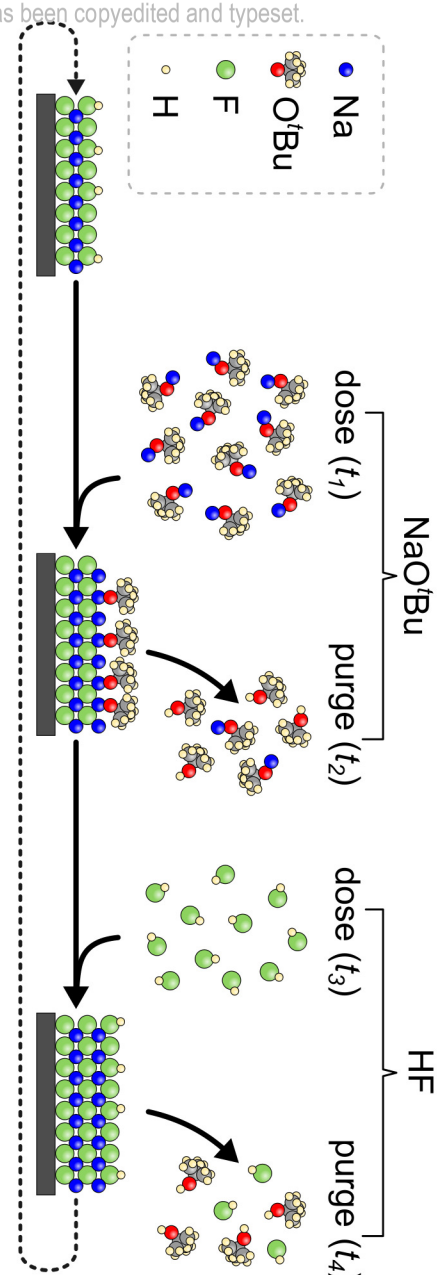

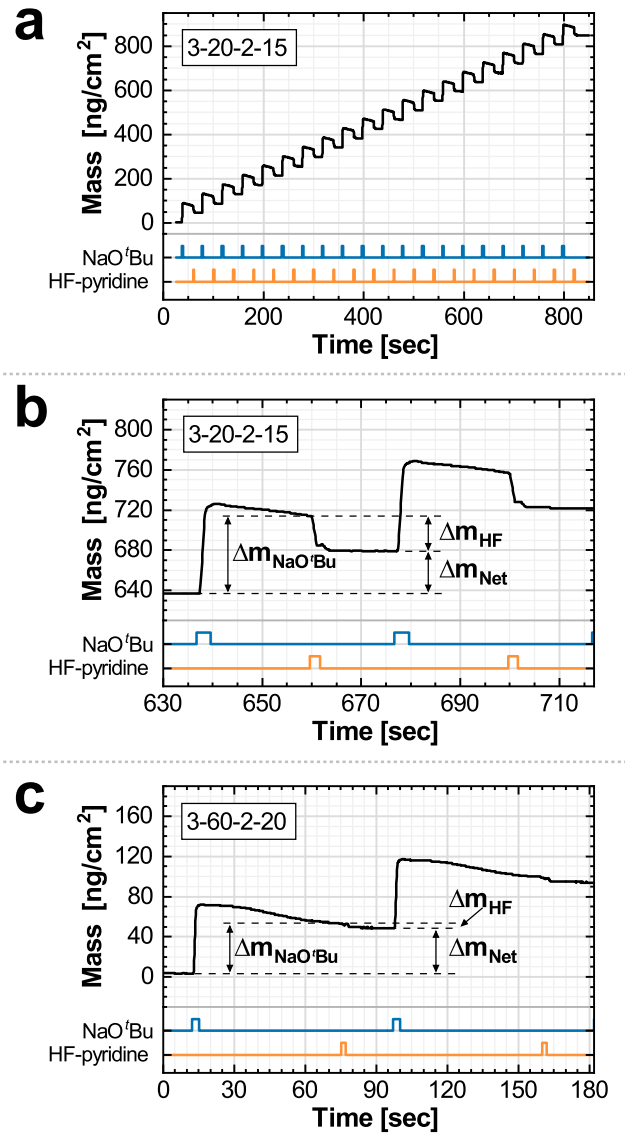

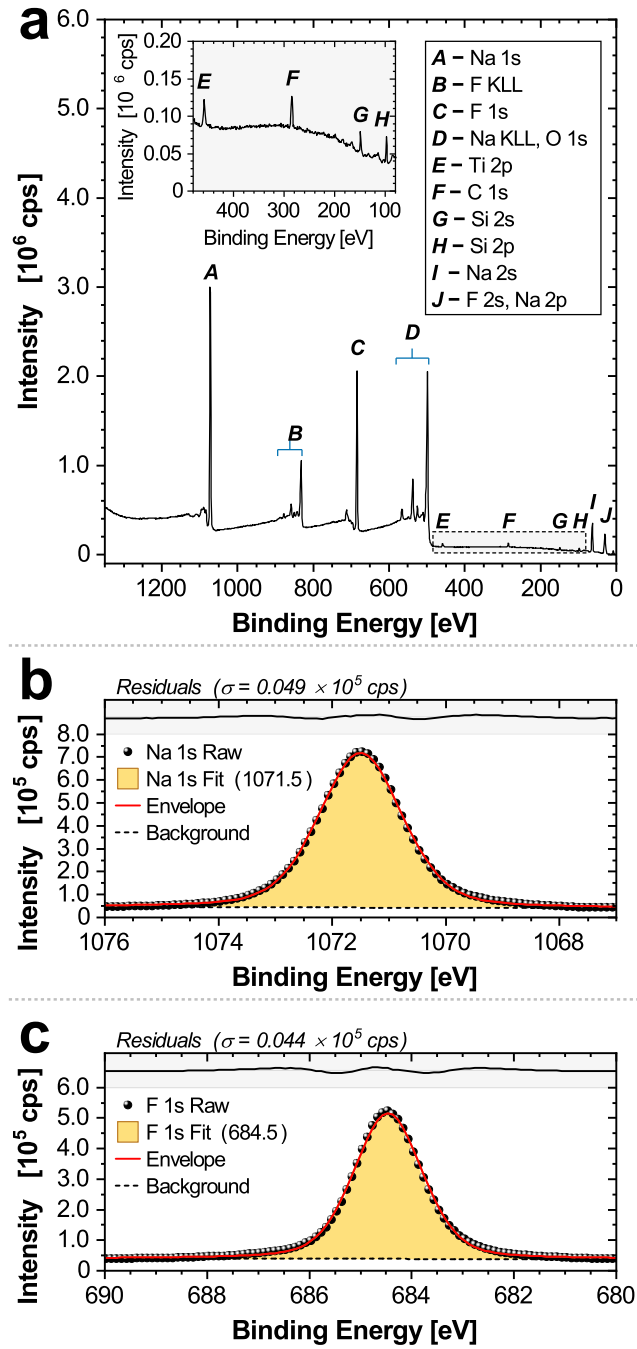

Journal of Vacuum Science Technology A

PLEASE CITE THIS ARTICLE AS DOI: 10.1116/6.0000847

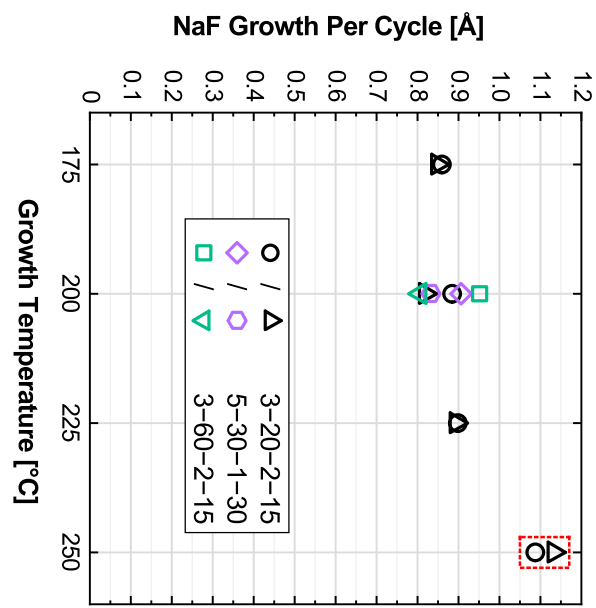

Journal of Vacuum Science Technology A

PLEASE CITE THIS ARTICLE AS DOI: 10.1116/6.0000847

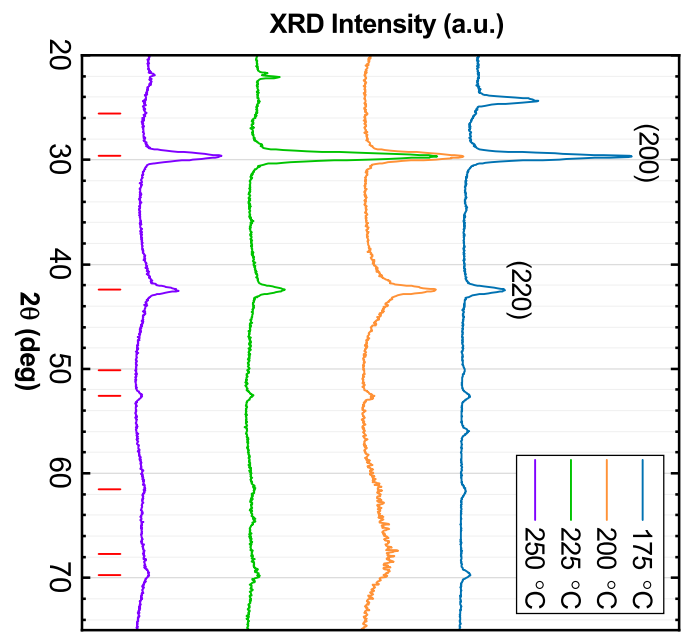

Journal of Vacuum Science Technology A